Supporting Information for

Unraveling the role of Fe and Ni in oxygen evolution reaction on pentlandite using three generations of computational surface models

Maksim Sokolov, Kai S. Exner*

*Email: kai.exner@uni-due.de

This PDF file includes:

Supporting text

Figures S1 to S3

Tables S1 to S6

SI References

S1 Justification for the surface-oxidized model

Apart from surface calculations, we also performed the formation energies of bulk oxides. We tested various configurations, one of which is shown in Figure S1. All of the structures with complete details are available in the data repository (1).

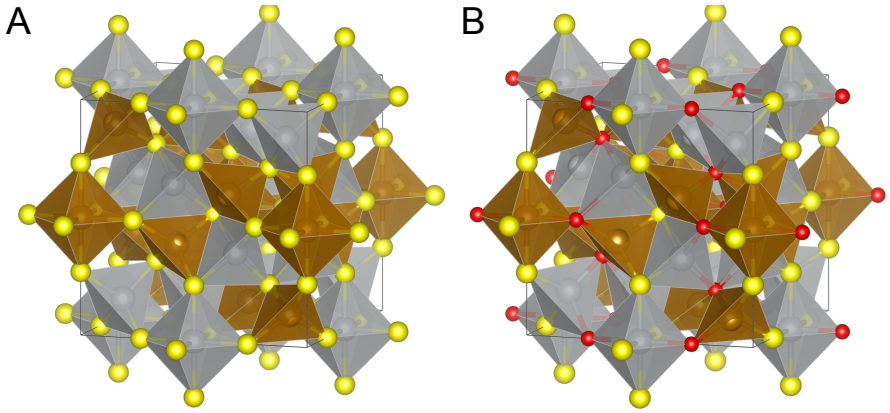

Figure S1. Bulk pentlandite structures. A: Pristine pentlandite; B: an example of oxidized pentlandite, where half of all sulfur atoms (all 8 in tetrahedral sites and 8 out of 24 in octahedral sites of the conventional unit cell) are substituted by oxygen atoms.

Table S1. Formation energies of different pentlandite oxides.

Index	N(O atoms)= θ	$N(O_{tet})$	$N(O_{oct})$	E_{form}	E_{form} / N(O atoms)
01	2	2	0	–6.51	–3.26
02	2	0	2	–5.18	–2.59
03	4	4	0	–13.29	–3.32
04	4	0	4	–10.57	–2.64
05	8	8	0	–26.41	–3.30
06	8	0	8	–21.10	–2.64
07	8	0	8	–20.29	–2.54
08	12	0	12	–33.44	–2.79
09	12	0	12	–31.13	–2.59
10	12	0	12	–31.11	–2.59
11	12	0	12	–32.31	–2.69
12	12	0	12	–31.80	–2.65
13	12	0	12	–32.15	–2.68
14	12	0	12	–31.88	–2.66
15	16	8	8	–49.86	–3.12
16	16	4	12	–45.89	–2.87

In order to model pentlandite oxidation, we assume the release of gaseous SO_2, which is a common product of sulfide oxidation in air. Using the equation

$$\mathrm{Fe_{4.5}Ni_{4.5}S_8} + 3\theta\mathrm{O_2} \rightarrow \mathrm{Fe_{4.5}Ni_{4.5}S_{8-\theta}O_\theta} + \theta\mathrm{SO_2(g)} \quad \text{(S1)}$$

, the formation energy E_{form} is defined as:

$$E_{\mathrm{form}} = E_{\mathrm{system}} + \theta E_{\mathrm{SO_2}} - 3\theta E_{\mathrm{O_2}} - E_{\mathrm{pristine}} \quad \text{(S2)}$$

As is evident from Table S1, the sulfur replacement to oxygen is favorable for pentlandite in air. Another interesting aspect is that the tetrahedral site is preferred over the octahedral one and that the average formation energy per oxygen atom barely increases with oxygen concentration. These findings corroborate our model for the pentlandite surface under OER conditions, where the sulfurs of two upper layers are replaced by oxygens, as described in the main text.

S2 Building the surface coverage

In this section, we describe all the steps required to move from the pristine surface (Figure 1 A,B in the main text) to the surface-oxidized Pourbaix-covered (SOPC) surface (Figure 1E-H in the main text). We begin with a surface-oxidized (SO) model (Figure 1C,D in the main text), in which we substitute the top half of the sulfur atoms in the pristine slab by oxygen atoms. This is justified by our data (cf. Table S1) and experimental observations that corroborate oxide formation in the top layers (2). The following procedure of building the Pourbaix coverage is reminiscent of the one developed in our previous work (3). We begin by investigating each potential reaction site by placing a single reaction intermediate of the mononuclear mechanism (cf. Equations (2)-(5) in the Methods section of the main text). Our calculations demonstrate that surface oxygen atoms do not participate in this process, and thus we identify 8 different metal adsorption sites, summarized in Table S2.

Using the framework of the computational hydrogen electrode (CHE) (4), we construct a Pourbaix diagram (5, 6), by evaluating the Gibbs adsorption free energy of the system at an applied electrode potential, $G_{\mathrm{ads}}(\mathrm{system})\ @\ U$, which can be expressed as:

$$G_{\mathrm{ads}}(\mathrm{system})\ @\ U = G_{\mathrm{system}} - G_{\mathrm{ref.surf.}} - n_{\mathrm{OH}}G_{\mathrm{OH}} - n_{\mathrm{O}}G_{\mathrm{O}} - n_e U \quad \text{(S3)}$$

Table S2 Stability of single reaction intermediates on different sites on the oxidized pentlandite. Columns "new reference" take into account the surface deformation that appears in the case of Ni_{tet2}-OH. Three lowest G_{ads} (defined in Equation S3) are highlighted in bold.

Adsorption site *M*	G_{ads}(M-OH) @ 0 V vs RHE	G_{ads}(M-O) @ 0 V vs RHE	G_{ads}(M-OOH) @ 0 V vs RHE	G_{ads}(M-OH) @ 1.23 V vs RHE, new reference	G_{ads}(M-O) @ 1.23 V vs RHE, new reference	G_{ads}(M-OOH) @ 1.23 V vs RHE, new reference,
Fe_{tet1}	–1.81	–0.33	1.78	1.10	1.35	2.24
Fe_{tet2}	–2.35	–1.74	0.16	0.56	–0.05	0.61
Ni_{tet1}	0.67	0.45	3.78	3.58	2.13	4.23
Ni_{tet2}	–3.54	0.44	–0.70	**–0.62**	2.13	–0.24
Fe_{hollow}	–1.30	–0.94	–1.32	1.61	0.75	**–0.86**
Ni_{hollow}	–0.81	1.54	2.68	2.10	3.23	3.14
Fe_{oct}	–1.34	–1.02	–1.13	1.57	0.67	**–0.67**
Ni_{oct}	–1.91	–1.20	1.29	1.01	0.48	1.74

We assume the zero-point energy E_{ZPE} and the entropy contribution TS can be neglected for the solid-state parts of the reaction. This is equivalent to a statement that G_{system} is equal to the computed DFT energy of the system with adsorbate/-s, $G_{\mathrm{ref.surf.}}$ is the computed DFT energy of the reference surface (i.e. surface without adsorbates). The other terms are defined as $G(\mathrm{OH}) = E_{\mathrm{DFT}}(\mathrm{H_2O}) + E_{\mathrm{ZPE}}(\mathrm{H_2O}) - TS(\mathrm{H_2O}) - \frac{1}{2}\left(E_{\mathrm{DFT}}(\mathrm{H_2}) + E_{\mathrm{ZPE}}(\mathrm{H_2}) - TS(\mathrm{H_2})\right)$ and $G_{\mathrm{O}} = E_{\mathrm{DFT}}(\mathrm{H_2O}) + E_{\mathrm{ZPE}}(\mathrm{H_2O}) - TS(\mathrm{H_2O}) - \left(E_{\mathrm{DFT}}(\mathrm{H_2}) + E_{\mathrm{ZPE}}(\mathrm{H_2}) - TS(\mathrm{H_2})\right)$, n_{OH} and n_{O} are the number of *M*-OH and *M*-O intermediates in the system, respectively (note that *M*-OOH is not included explicitly, since it is energetically equivalent to a combination of a single *M*-OH and single *M*-O intermediate). $n_e = n_{\mathrm{OH}} + 2n_{\mathrm{O}}$ is the total number of electrons transferred for the hypothetical transformation from the reference surface to the system.

An unusually low adsorption energy is observed for the $\mathrm{Ni_{tet2}}$-OH intermediate, which, upon visual inspection, appeared to be a noticeable surface reconstruction. By removing the adsorbate from the converged structure and re-optimizing the structure again, it was confirmed that the introduced deformation are stable and provide a structure that is more energetically favorable than the initial reference. For further calculations, the new reference was used.

To determine the surface coverage, three structures were used as starting points: $\mathrm{Ni_{tet2}}$-OH, $\mathrm{Fe_{hollow}}$-OOH, and $\mathrm{Fe_{oct}}$-OOH, as they are the lowest in free energy at the OER equilibrium overpotential of $U_0^{\mathrm{OER}} = 1.23\ \mathrm{V\ vs\ RHE}$. Interestingly, both $\mathrm{Fe_{hollow}}$-OOH and $\mathrm{Fe_{oct}}$-OOH demonstrate OOH intermediate dissociation to adjacent O and OH intermediates. The stable OOH intermediate is only observed for $\mathrm{Ni_{tet2}}$ and $\mathrm{Fe_{tet2}}$, similarly to the case of the pristine and Pourbaix-covered (PC) pentlandite surface (first- and second-generation model, respectively).

The further procedure constitutes combining the three converged structures and iteratively adding more OH or O intermediates to the structure based on observed energetics and structure transformations. The data is summarized in Table S3. We also included intermediates on $\mathrm{Ni_{oct}}$ in the initial analysis, but it showed less favorable energetics and was excluded from further iterations. This procedure culminates in the Pourbaix diagram, shown in Figure S2, where the determined coverage is 6*M*-O+2*M*-OH.

As more adsorbates are introduced into the system, the symmetry of the slab breaks, and the sites that were equivalent in the pristine or PC surface (compare the sites in Figure 1E and Figure 1G of the main text) are no longer such. To account for this finding, the OER was modelled on each of the newly formed $\mathrm{Ni_{tet2}}$ and $\mathrm{Fe_{tet2}}$ sites.

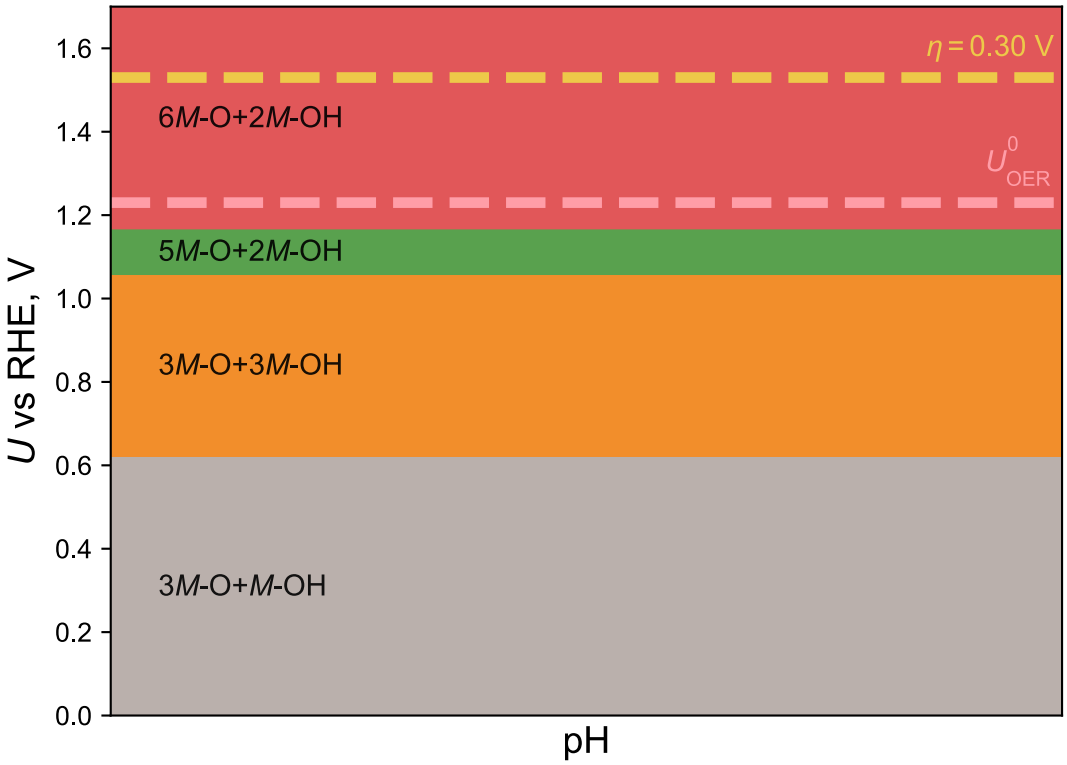

Figure S2. Pourbaix diagram for the surface-oxidized (SO) pentlandite. The top red region corresponds to the surface-oxidized Pourbaix-covered (SOPC) pentlandite. This surface coverage is used in the main text for further analysis.

Table S3. Stability of different coverages of the oxidized pentlandite model.

Index	Index of the source surface	Additional RI/-s	Total coverage (*M*-OH+*M*-O)	G_{ads} @ 0V vs RHE	G_{ads} @ 1.23V vs RHE
00[1]	-	-	0	0.00	0.00
01[2]	00	Ni_{tet2}-OH	1+0	0.61	–0.62
02[3]	00	Fe_{hollow}-OOH	1+1	2.83	–0.86
03[4]	00	Fe_{oct}-OOH	1+1	3.02	–0.67
04[5]	01	Fe_{tet2}-OH + Fe_{hollow}-O	2+1	3.37	–1.55
05	02	Ni_{oct}-OH	2+1	2.71	–2.21
06	02	Fe_{tet2}-O	1+2	3.07	–3.08
07	02	Ni_{oct}-O	1+2	3.69	–2.46
08[6]	01	Ni_{tet2}-OH + Fe_{oct}-O	2+1	0.89	**–4.03**
09	03	Fe_{tet2}-OH	2+1	3.83	–1.09
10	03	Fe_{tet2}-O	1+2	4.23	–1.92
11	03	Ni_{oct}-O	1+2	6.06	–0.09
12[7]	03	Fe_{tet2}-OH + Fe_{hollow}-O	2+2	4.63	–2.75
13	08	Fe_{oct}-O	2+2	0.19	**–7.19**
14	08	Fe_{tet2}-O	2+2	1.27	–6.11
15	08	Fe_{tet2}-OH	3+1	–0.67	–6.82
16	08	Fe_{hollow}-O	2+2	1.80	–5.58
17	13	Fe_{tet2}-O	2+3	1.23	–8.61
18	13	Fe_{tet2}-OH	3+2	0.77	–7.84
19	17	Fe_{tet2}-O	2+4	2.92	–9.38
20	17	Fe_{tet2}-OH	3+3	1.83	–9.24
21	18	Fe_{tet2}-O	3+3	2.52	–8.55
22	18	Fe_{tet2}-OH	4+2	1.44	–8.40
23	19	Fe_{tet2}-O	2+5	5.00	–9.76
24	19	Fe_{tet2}-O + Fe_{tet2}-O	2+6	7.34	–9.88

[1] Reference, reoptimized from 3 after removing Ni_{tet2}-OH reaction intermediate

[2] Surface reconstruction observed, reference readjusted to take ignore the deformation energy

[3] Dissociation to Fe_{tet2}-OH + Fe_{hollow}-O

[4] Dissociation to Ni_{tet2}-OH + Fe_{oct}-O

[5] combination of 1 and 2

[6] Combination of 1 and 3

[7] Combination of 2 and 3

S3 Thermodynamics of the OER on PC and SOPC surfaces

We modeled all of the mechanisms described in the Methods section of the main text on Ni_{tet2} and Fe_{tet2} sites of PC and SOPC surfaces (two distinct Ni_{tet2} and four distinct Fe_{tet2} sites for SOPC surface). The data is summarized in Table S4 and visualized in free energy diagrams (FEDs) in Figure S3. The oxide mechanism on the PC surface is not present in the analysis as we were unable to find two stable adjacent *M*-OO intermediates. Two versions of the binuclear mechanism on the SOPC surface constitute different orders of *M*-OH formation. Two versions of bifunctional I, II, and bifunctional-Walden mechanism are due to two adjacent oxygens $*O_A$ (see the structures in the data repository (1) for more details).

Table S4 Electrocatalytic activity based on the activity descriptor $G_{\max}(0.30\ \mathrm{V})$ for different surfaces, sites, and mechanisms.

Index	Source surface structure	Adsorption Site	Mechanism	$G_{\max}(0.30\ \mathrm{V})$, eV	Determining span
01	Pristine 20*O covered	Fe_{tet2}	Mononuclear (3)	0.40	*M*-OH → *M* + O_2(*g*)
02	Pristine 20*O covered	Fe_{tet2}	Bifunctional I	0.58	*M*-OH + $*O_A$ → *M*-OO + $*O_AH$
03	Pristine 20*O covered	Fe_{tet2}	Bifunctional II	0.94	*M*-OH + $*O_A$ → *M*-OOH + $*O_AH$
04	Pristine 20*O covered	Fe_{tet2}	Mononuclear-Walden	0.17	*M*-OH → *M*-OOH
05	Pristine 20*O covered	Fe_{tet2}	Bifunctional-Walden	0.58	*M*-OH + $*O_A$ → *M*-OO + $*O_AH$
06	Pristine 20*O covered	Ni_{tet2}	Mononuclear (3)	0.64	*M*-O → *M*-OOH
07	Pristine 20*O covered	Ni_{tet2}	Bifunctional I	1.02	*M*-O → *M*-OO + $*O_AH$
08	Pristine 20*O covered	Ni_{tet2}	Bifunctional II	1.63	*M*-O + $*O_A$ → *M*-OOH + $*O_AH$
09	Pristine 20*O covered	Ni_{tet2}	Mononuclear-Walden	0.64	*M*-O → M-OOH
10	Pristine 20*O covered	Ni_{tet2}	Bifunctional-Walden	1.02	*M*-O + $*O_A$ → *M*-OO + $*O_AH$
11	Pristine 20*O covered	Fe_{tet2}-Ni_{tet1}	Binuclear	0.86	*M*-O + *M*-O → *M* + *M* + O_2(g)
12	Oxidized 6*O+2*OH covered	$Fe_{tet2,1}$	Mononuclear	1.39	*M*-OOH → *M* + O_2(g)
13	Oxidized 6*O+2*OH covered	$Fe_{tet2,2}$	Mononuclear	2.66	*M*-OOH → *M* + O_2(*g*)
14	Oxidized 6*O+2*OH covered	$Fe_{tet2,3}$	Mononuclear	0.52	*M*-OOH → *M* + O_2(g)
15	Oxidized 6*O+2*OH covered	$Fe_{tet2,4}$	Mononuclear	0.59	*M*-OH → *M*-O
16	Oxidized 6*O+2*OH covered	$Fe_{tet2,3}$	Bifunctional I	0.47	*M*-O → *M* + O_2(g)
17	Oxidized 6*O+2*OH covered	$Fe_{tet2,3}$	Bifunctional II	0.71	*M*-O + $*O_A$ → *M*-OOH + $*O_AH$
18	Oxidized 6*O+2*OH covered	$Fe_{tet2,1}$-$Fe_{tet2,4}$	Binuclear	1.80	*M*-O + *M*-OH → *M* + *M* + O_2(g)
19	Oxidized 6*O+2*OH covered	$Fe_{tet2,1}$-$Fe_{tet2,4}$ v2	Binuclear	1.21	*M*-O + *M*-O → *M* + *M* + O_2(g)
20	Oxidized 6*O+2*OH covered	$Fe_{tet2,3}$-$Fe_{tet2,4}$	Oxide	0.89	*M*-OO + *M*-OO → *M*-O + *M*-O + O_2(g)
21	Oxidized 6*O+2*OH covered	$Fe_{tet2,3}$-$Fe_{tet2,4}$	Oxide	0.89	*M*-OO + *M*-OO → *M*-O + *M*-O + O_2(g)
22	Oxidized 6*O+2*OH covered	$Fe_{tet2,1}$	Mononuclear-Walden	0.48	*M*-OOH → *M*-OO
23	Oxidized 6*O+2*OH covered	$Fe_{tet2,2}$	Mononuclear-Walden	2.55	*M*-OOH → *M*-OO
24	Oxidized 6*O+2*OH covered	$Fe_{tet2,3}$	Mononuclear-Walden	0.36	*M*-OO → *M*-OH + O_2(g)
25	Oxidized 6*O+2*OH covered	$Fe_{tet2,4}$	Mononuclear-Walden	0.59	*M*-OH → M-O
26	Oxidized 6*O+2*OH covered	$Fe_{tet2,3}$	Bifuncitonal-Walden	0.36	*M*-OO + $*O_A$ → *M*-OH + $*O_A$ + O_2(g)
27	Oxidized 6*O+2*OH covered	$Ni_{tet2,1}$	Mononuclear	0.22	*M*-OH → *M*-O
28	Oxidized 6*O+2*OH covered	$Ni_{tet2,2}$	Mononuclear	1.51	*M*-O → *M* + O_2(g)
29	Oxidized 6*O+2*OH covered	$Ni_{tet2,1}$	Bifuncitonal I	2.77	*M*-OO + $*O_AH$ → *M* + $*O_A$ + O_2(*g*)
30	Oxidized 6*O+2*OH covered	$Ni_{tet2,1}$ v2	Bifunctional I	1.23	*M*-OO + $*O_AH$ → *M* + $*O_A$ + O_2(*g*)
31	Oxidized 6*O+2*OH covered	$Ni_{tet2,2}$	Bifuncitonal I	1.93	*M*-O + $*O_A$ → *M*-OO + $*O_AH$
32	Oxidized 6*O+2*OH covered	$Ni_{tet2,1}$	Bifuncitonal II	2.49	*M*-OOH + $*O_AH$ → *M*-OOH + $*O_A$
33	Oxidized 6*O+2*OH covered	$Ni_{tet2,1}$ v2	Bifunctional II	0.22	*M*-OH + $*O_A$ → *M*-O + $*O_A$
34	Oxidized 6*O+2*OH covered	$Ni_{tet2,2}$	Bifuncitonal II	1.93	*M*-O + $*O_A$ → *M*-OOH+$*O_AH$
35	Oxidized 6*O+2*OH covered	$Ni_{tet2,1}$	Mononuclear-Walden	0.22	*M*-OH → *M*-O
36	Oxidized 6*O+2*OH covered	$Ni_{tet2,2}$	Mononuclear-Walden	0.73	*M*-O → *M*-OOH
37	Oxidized 6*O+2*OH covered	$Ni_{tet2,1}$	Bifuncitonal-Walden	2.39	*M*-OO + $*O_AH$ → *M*-OO + $*O_A$
38	Oxidized 6*O+2*OH covered	$Ni_{tet2,1}$ v2	Bifuncitonal-Walden	0.85	*M*-OO + $*O_AH$ → *M*-OO + $*O_A$

In Table S5, we demonstrate the applicability of the assumption that the vibrational contributions E_{ZPE} and TS_{vib} can be neglected for the surface configurations. E_{ZPE} and TS_{vib} were calculated using the finite-differences method in VASP by keeping only the bottom slab layer frozen. We obtain only a significant quantitative difference for index 08, where the difference in $G_{\max}(0.30\ \mathrm{V})$ amounts to 0.57 eV and the initial adsorbate governing the determining span shifts from *M*-OH to *M*-O for Fe. However, based on the $G_{\max}(0.30\ \mathrm{V})$ value exceeding 1 eV by far, this surface site is inactive and does not play a role in OER. More precisely, there is neither a single case where the inclusion of E_{ZPE} and TS_{vib} changes the energetics or determining span significantly for an active site in OER nor a case where the classification between an active and inactive site (according to the $G_{\max}(0.30\ \mathrm{V}) < 0.55\ \mathrm{eV}$ criterion) is affected. Therefore, this finding confirms to perform Gibbs free energy calculations for the SOPC surface without accounting for the E_{ZPE} and TS_{vib} terms.

Table S5 Electrocatalytic activity based on the activity descriptor $G_{\max}(0.30\ \mathrm{V})$ for different surfaces, sites, and mechanisms. Comparison of $G_{\max}(0.30\ \mathrm{V})$ with and without the vibrational contributions E_{ZPE} and TS_{vib}. The index column refers to Table S4.

Index	$G_{\max}(0.30\ \mathrm{V})$, **without** vibrational contributions eV	Determining span, **without** vibrational contributions	$G_{\max}(0.30\ \mathrm{V})$, **with** vibrational contributions eV	Determining span, **with** vibrational contributions
01	0.40	*M*-OH → *M* + $O_2(g)$	0.11	*M*-O → *M* + $O_2(g)$
02	0.58	*M*-OH + *O_A → *M*-OO + *O_AH	0.62	*M*-O + *O_A → *M*-OO + *O_AH
03	0.94	*M*-OH + *O_A → *M*-OOH + *O_AH	1.34	*M*-O + *O_A → *M*-OOH + *O_AH
04	0.17	*M*-OH → *M*-OOH	0.05	*M*-O → *M*-OOH
05	0.58	*M*-OH + *O_A → *M*-OO + *O_AH	0.62	*M*-O + *O_A → *M*-OO + *O_AH
06	0.64	*M*-O → *M*-OOH	0.82	*M*-O → *M*-OOH
07	1.02	*M*-O → *M*-OO + *O_AH	1.18	*M*-O → *M*-OO + *O_AH
08	1.63	*M*-O + *O_A → *M*-OOH + *O_AH	2.20	*M*-O + *O_A → *M*-OOH + *O_AH
09	0.64	*M*-O → M-OOH	0.82	*M*-O → M-OOH
10	1.02	*M*-O + *O_A → *M*-OO + *O_AH	1.18	*M*-O + *O_A → *M*-OO + *O_AH
11	0.86	*M*-O + *M*-O → *M* + *M* + O_2(g)	0.72	*M*-O + *M*-O → *M* + *M* + O_2(g)

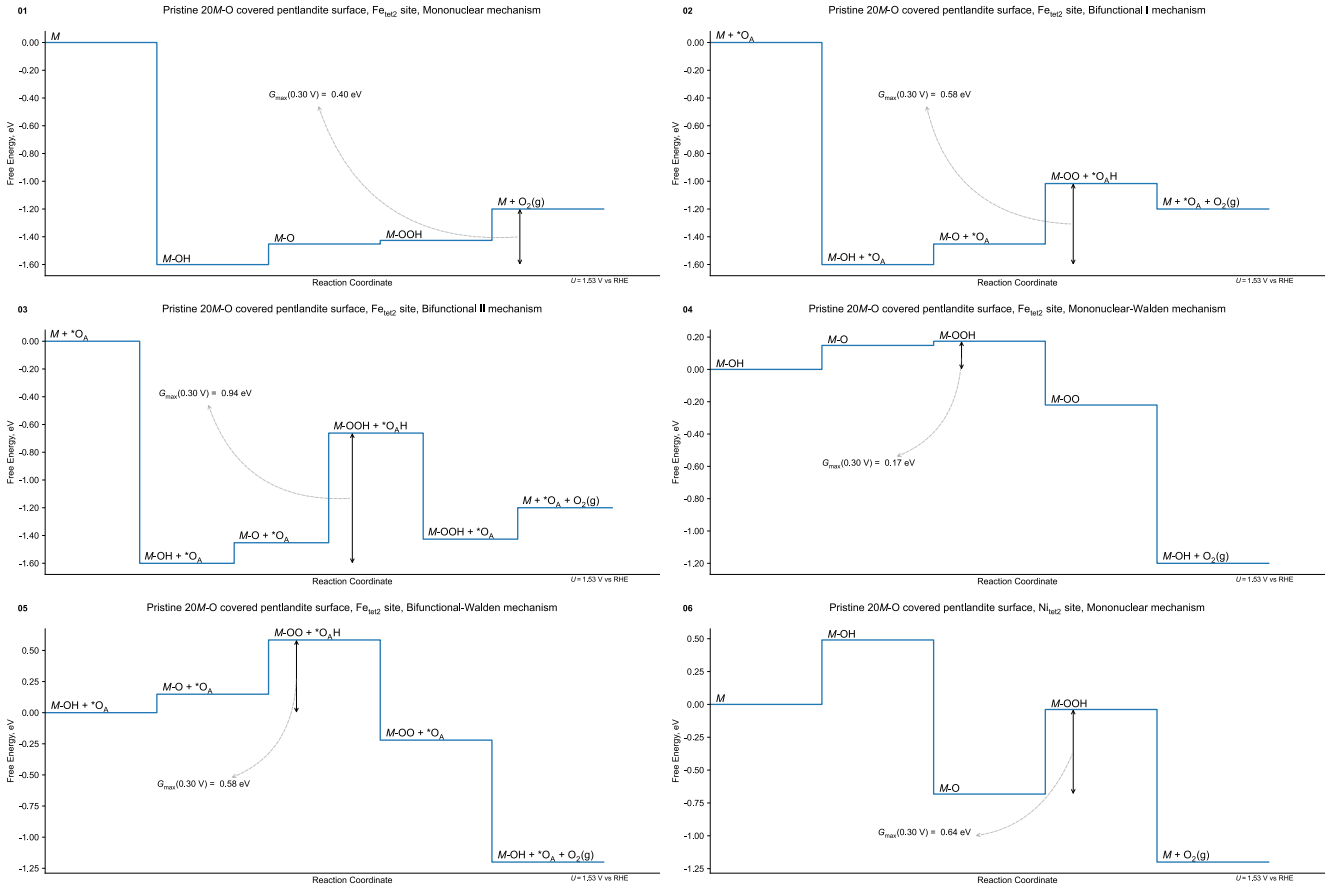

07

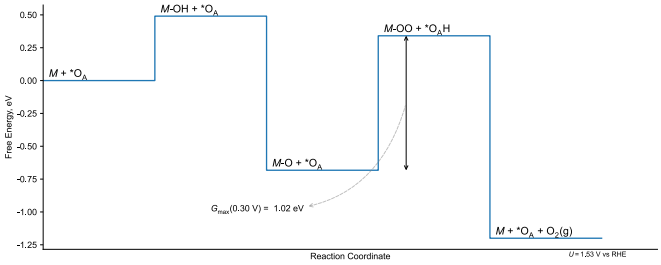

08

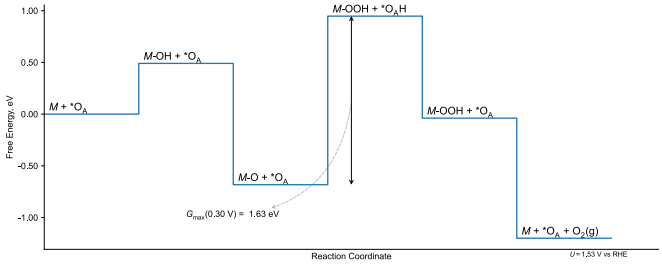

09

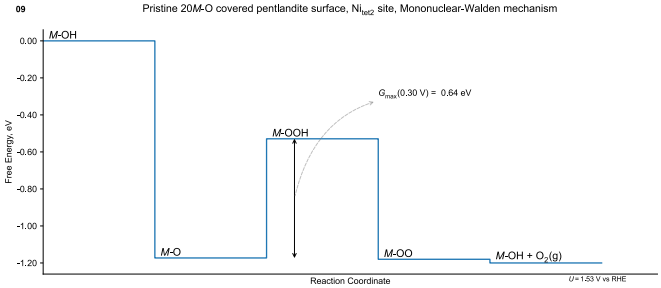

10

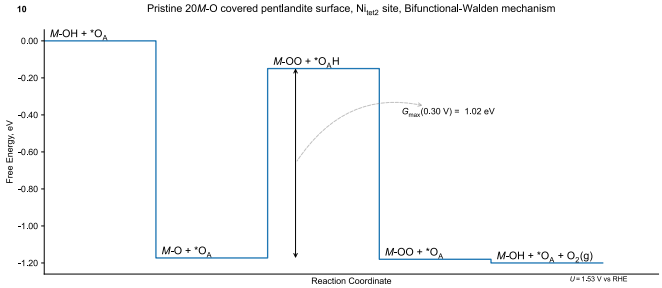

11

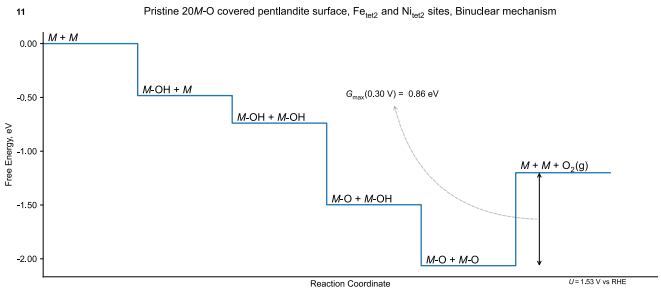

12

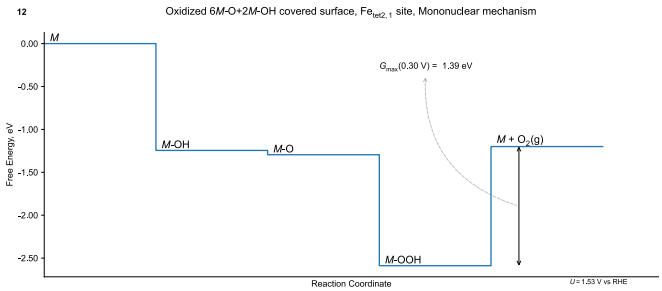

13

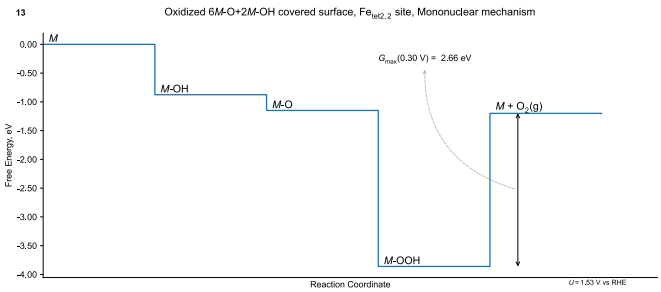

14

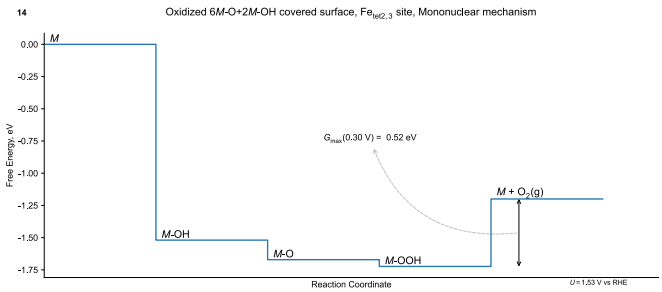

15

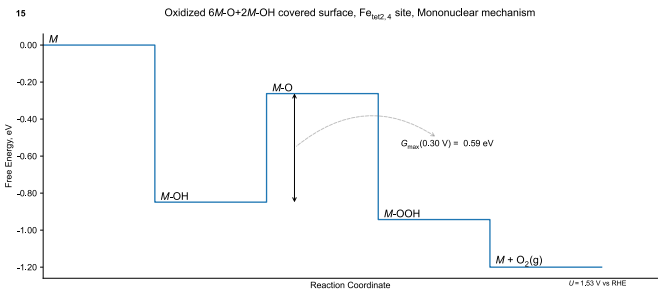

16

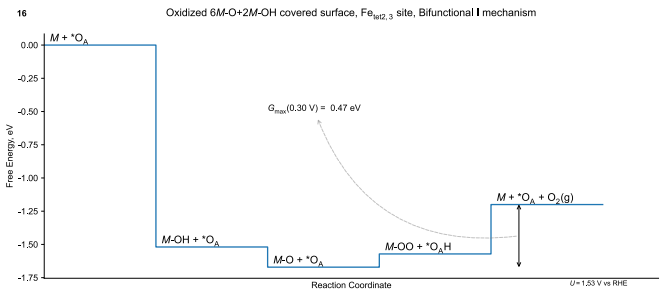

17

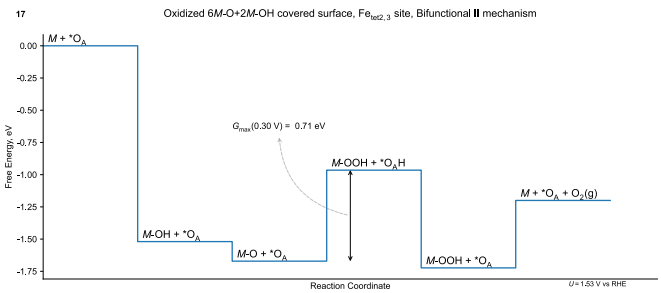

18

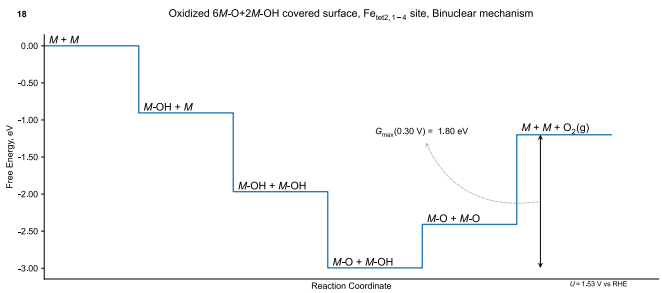

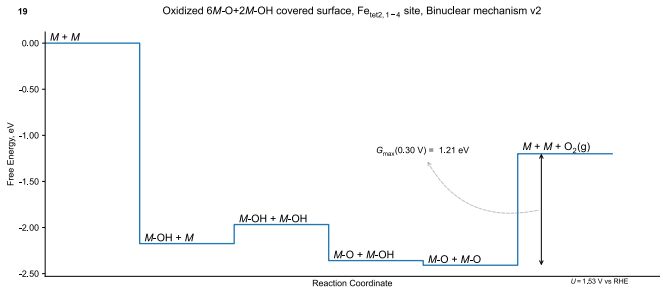
19
Oxidized 6M-O+2M-OH covered surface, Fetet2, 1−4 site, Binuclear mechanism v2
M + M
M-OH + M
M-OH + M-OH
M-O + M-OH
M-O + M-O
M + M + O2(g)
Gmax(0.30 V) = 1.21 eV
Free Energy, eV
Reaction Coordinate
U = 1.53 V vs RHE

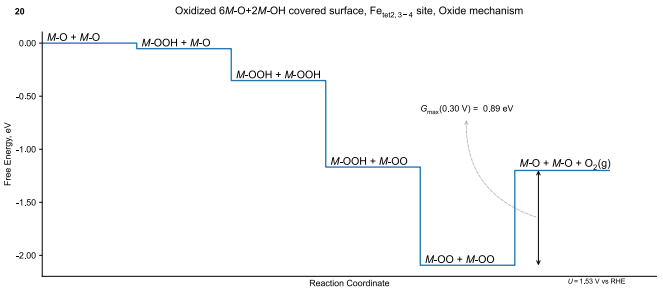
20
Oxidized 6M-O+2M-OH covered surface, Fetet2, 3−4 site, Oxide mechanism
M-O + M-O
M-OOH + M-O
M-OOH + M-OOH
M-OOH + M-OO
M-OO + M-OO
M-O + M-O + O2(g)
Gmax(0.30 V) = 0.89 eV
Free Energy, eV
Reaction Coordinate
U = 1.53 V vs RHE

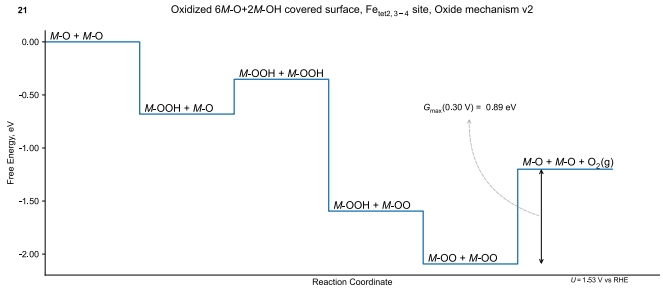
21
Oxidized 6M-O+2M-OH covered surface, Fetet2, 3−4 site, Oxide mechanism v2
M-O + M-O
M-OOH + M-O
M-OOH + M-OOH
M-OOH + M-OO
M-OO + M-OO
M-O + M-O + O2(g)
Gmax(0.30 V) = 0.89 eV
Free Energy, eV
Reaction Coordinate
U = 1.53 V vs RHE

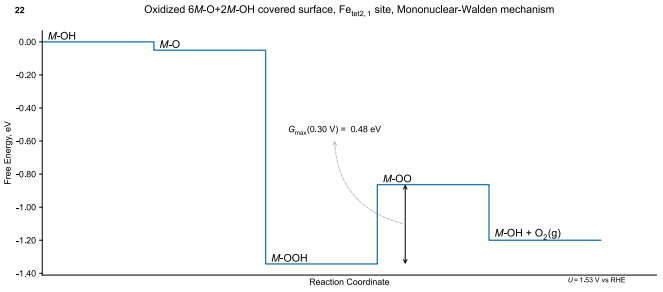
22
Oxidized 6M-O+2M-OH covered surface, Fetet2, 1 site, Mononuclear-Walden mechanism
M-OH
M-O
M-OOH
M-OO
M-OH + O2(g)
Gmax(0.30 V) = 0.48 eV
Free Energy, eV
Reaction Coordinate
U = 1.53 V vs RHE

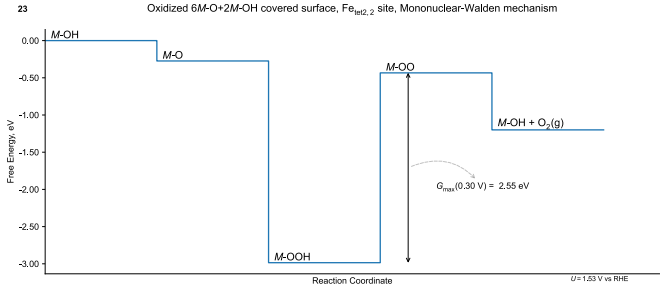
23
Oxidized 6M-O+2M-OH covered surface, Fetet2, 2 site, Mononuclear-Walden mechanism
M-OH
M-O
M-OOH
M-OO
M-OH + O2(g)
Gmax(0.30 V) = 2.55 eV
Free Energy, eV
Reaction Coordinate
U = 1.53 V vs RHE

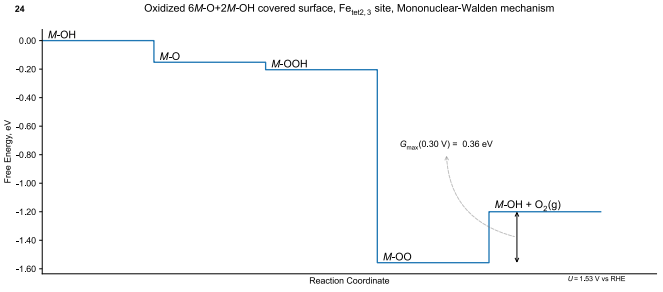
24
Oxidized 6M-O+2M-OH covered surface, Fetet2, 3 site, Mononuclear-Walden mechanism
M-OH
M-O
M-OOH
M-OO
M-OH + O2(g)
Gmax(0.30 V) = 0.36 eV
Free Energy, eV
Reaction Coordinate
U = 1.53 V vs RHE

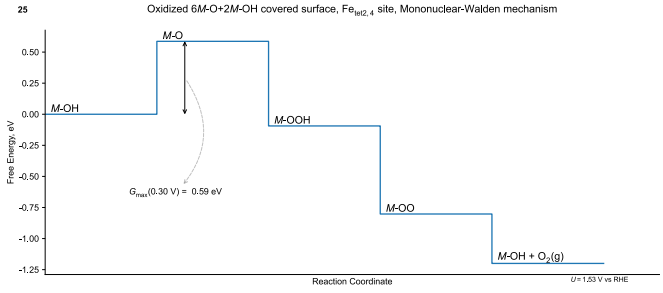
25
Oxidized 6M-O+2M-OH covered surface, Fetet2, 4 site, Mononuclear-Walden mechanism
M-O
M-OH
M-OOH
M-OO
M-OH + O2(g)
Gmax(0.30 V) = 0.59 eV
Free Energy, eV
Reaction Coordinate
U = 1.53 V vs RHE

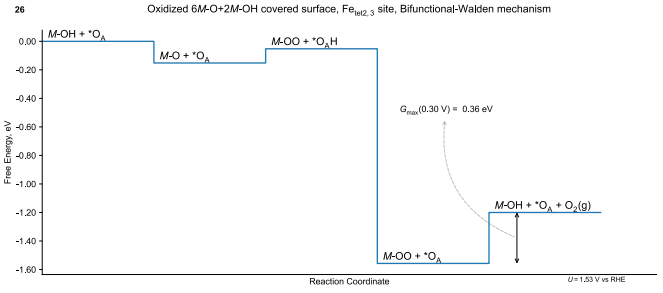
26
Oxidized 6M-O+2M-OH covered surface, Fetet2, 3 site, Bifunctional-Walden mechanism
M-OH + *OA
M-O + *OA
M-OO + *OAH
M-OO + *OA
M-OH + *OA + O2(g)
Gmax(0.30 V) = 0.36 eV
Free Energy, eV
Reaction Coordinate
U = 1.53 V vs RHE

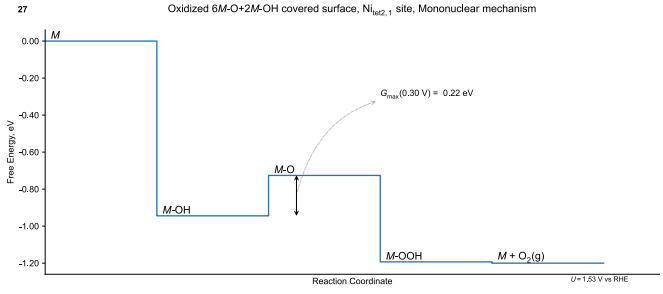
27
Oxidized 6M-O+2M-OH covered surface, Nitet2, 1 site, Mononuclear mechanism
M
M-OH
M-O
M-OOH
M + O2(g)
Gmax(0.30 V) = 0.22 eV
Free Energy, eV
Reaction Coordinate
U = 1.53 V vs RHE

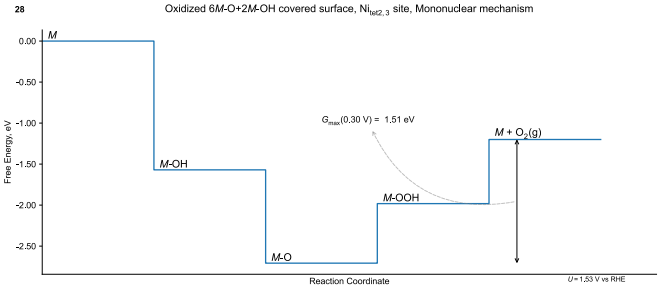
28
Oxidized 6M-O+2M-OH covered surface, Nitet2, 3 site, Mononuclear mechanism
M
M-OH
M-O
M-OOH
M + O2(g)
Gmax(0.30 V) = 1.51 eV
Free Energy, eV
Reaction Coordinate
U = 1.53 V vs RHE

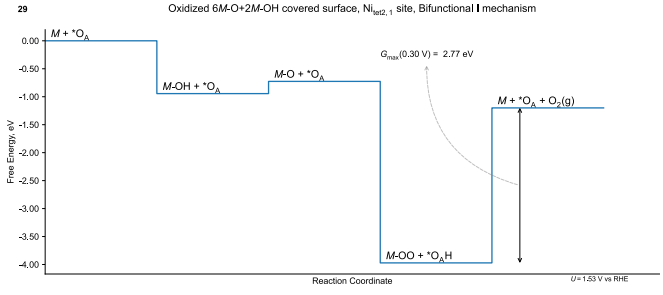
29
Oxidized 6M-O+2M-OH covered surface, Nitet2, 1 site, Bifunctional I mechanism
M + *OA
M-OH + *OA
M-O + *OA
M-OO + *OAH
M + *OA + O2(g)
Gmax(0.30 V) = 2.77 eV
Free Energy, eV
Reaction Coordinate
U = 1.53 V vs RHE

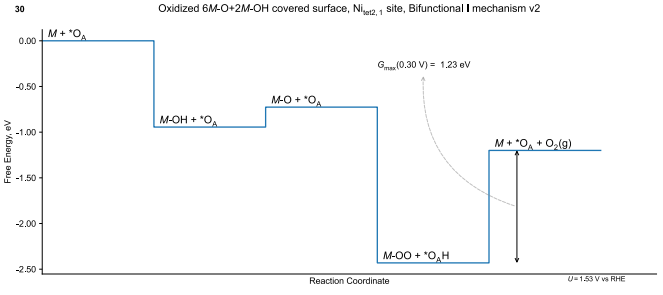
30
Oxidized 6M-O+2M-OH covered surface, Nitet2, 1 site, Bifunctional I mechanism v2
M + *OA
M-OH + *OA
M-O + *OA
M-OO + *OAH
M + *OA + O2(g)
Gmax(0.30 V) = 1.23 eV
Free Energy, eV
Reaction Coordinate
U = 1.53 V vs RHE

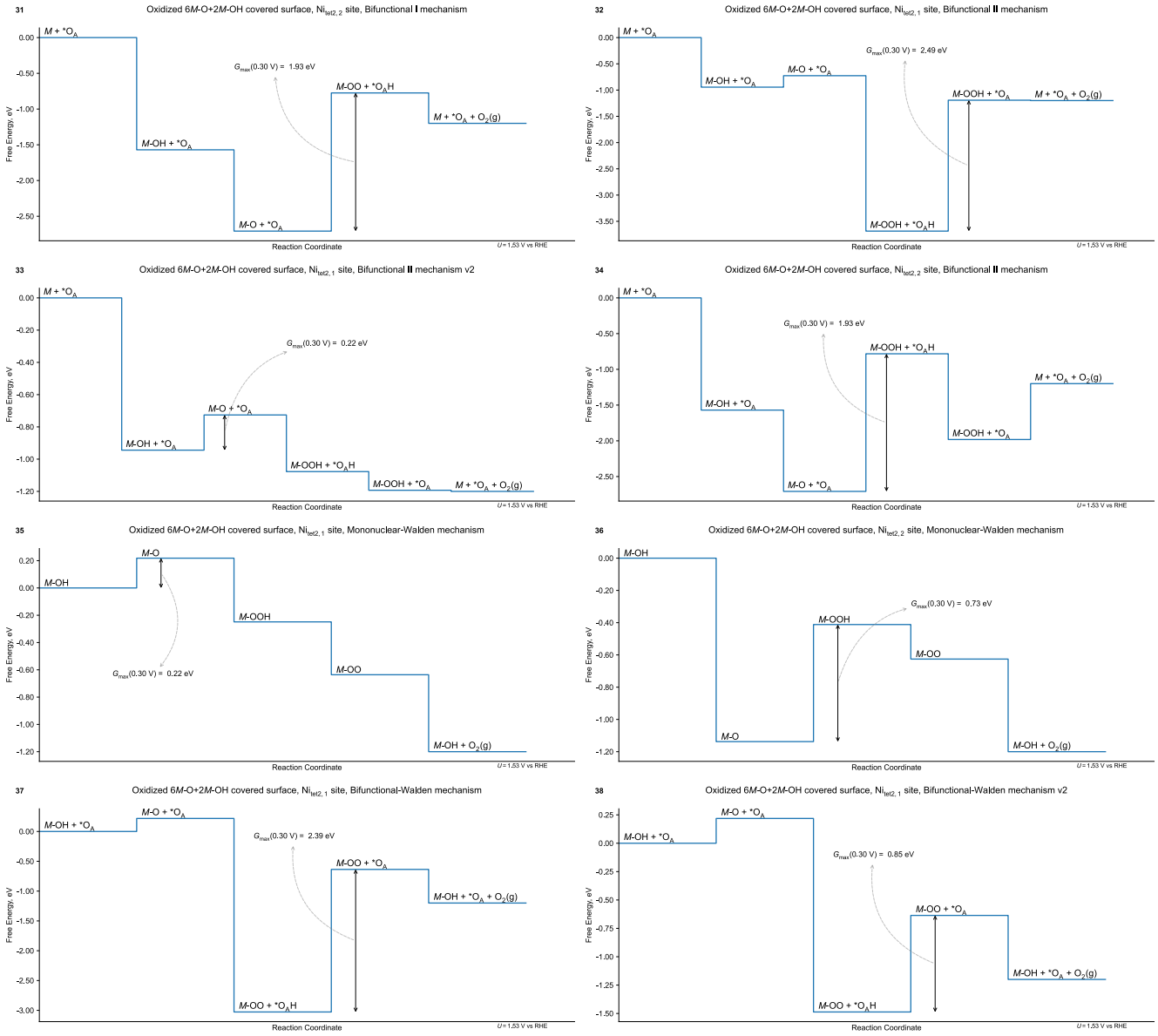

Figure S3. All Free-energy diagrams (FEDs) for different OER mechanisms on different pentlandite models. Indices 1-38 correspond to the records in Table S4 and the data repository. Data for the mononuclear mechanism on the SO surface is taken from (2).

S4 Computational details

Table S4 below comprises a comprehensive description of computational parameters used in the present calculations. For the complete VASP setup, please refer to the data repository (1).

Table S6. Complete list of computational parameters used for all calculations.

Software	VASP 6.3.0 and 6.4.1 (40)
Exchange-correlation functional	PBE (7) for bulk oxidation, RPBE (8) for surface calculations
Pseudopotentials	Ultrasoft potentials (9) using projector augmented wave (PAW) (10) method
Fe valence configuration	$3d^7 4s^1$, valence 8, energy cutoff 268 eV, generated 06.09.2000
Ni valence configuration	unspecified configuration, valence 10, energy cutoff 270 eV, generated 06.09.2000
S valence configuration	$3s^2 3p^4$, valence 6, energy cutoff 400 eV, generated 17.01.2003
O valence configuration	$2s^2 2p^4$, valence 6, energy cutoff 400 eV, generated 08.04.2002
H valence configuration	$1s^1$, valence 1, energy cutoff 250 eV, gen- erated 15.06.2001
Spin polarization	Non-spin polarized calculations
Plane wave cut-off	500 eV
Smearing	Gaussian smearing
Dispersion correction	Grimme DFT-D3 correction (11) with Becke-Johnson damping (12)
Self-consistent field convergence criteria	Energy difference between iterations is less than 10^{-4} eV
Geometry convergence criteria	Forces are smaller than 0.05 eV $Å^{-1}$ (0.06 eV $Å^{-1}$ for oxidized surfaces). Bottom-most layer frozen.
k-points	$6 \times 6 \times 1$ for surface calculations, $8 \times 8 \times 8$ for bulk, Γ-centered

References

1. M. Sokolov, Kai S. Exner, Data repository and scripts for the OER on pentlandite DFT calculations. https://doi.org/10.5281/zenodo.15723787. Deposited 23 June 2025.

2. H. M. A. Amin, M. Attia, D. Tetzlaff, U. Apfel, Tailoring the Electrocatalytic Activity of Pentlandite Fe x Ni 9-X S 8 Nanoparticles via Variation of the Fe : Ni Ratio for Enhanced Water Oxidation. *ChemElectroChem* **8**, 3863–3874 (2021).

3. M. Sokolov, K. Doblhoff-Dier, K. S. Exner, Best practices of modeling complex materials in electrocatalysis, exemplified by oxygen evolution reaction on pentlandites. *Phys. Chem. Chem. Phys.* **26**, 22359–22370 (2024).

4. J. K. Nørskov, *et al.*, Origin of the overpotential for oxygen reduction at a fuel-cell cathode. *Journal of Physical Chemistry B* **108**, 17886–17892 (2004).

5. H. A. Hansen, J. Rossmeisl, J. K. Nørskov, Surface Pourbaix diagrams and oxygen reduction activity of Pt, Ag and Ni(111) surfaces studied by DFT. *Phys. Chem. Chem. Phys.* **10**, 3722 (2008).

6. M. López, K. S. Exner, F. Viñes, F. Illas, Computational Pourbaix Diagrams for MXenes: A Key Ingredient toward Proper Theoretical Electrocatalytic Studies. *Advcd Theory and Sims* 2200217 (2022). https://doi.org/10.1002/adts.202200217.

7. J. P. Perdew, K. Burke, M. Ernzerhof, Generalized Gradient Approximation Made Simple. *Physical Review Letters* **77**, 3865–3868 (1996).

8. B. Hammer, L. B. Hansen, J. K. Nørskov, Improved adsorption energetics within density-functional theory using revised Perdew-Burke-Ernzerhof functionals. *Phys. Rev. B* **59**, 7413–7421 (1999).

9. G. Kresse, D. Joubert, From ultrasoft pseudopotentials to the projector augmented-wave method. *Physical Review B* **59**, 1758–1775 (1999).

10. P. E. Blöchl, Projector augmented-wave method. *Physical Review B* **50**, 17953–17979 (1994).

11. S. Grimme, J. Antony, S. Ehrlich, H. Krieg, A consistent and accurate *ab initio* parametrization of density functional dispersion correction (DFT-D) for the 94 elements H-Pu. *The Journal of Chemical Physics* **132**, 154104 (2010).

12. S. Grimme, S. Ehrlich, L. Goerigk, Effect of the damping function in dispersion corrected density functional theory. *J Comput Chem* **32**, 1456–1465 (2011).